CrossMark

Crossing the Rubicon of Reionization with $z \sim 5$ QSOs

Andrea Grazian[1] , Konstantina Boutsia[2] , Emanuele Giallongo[3] , Stefano Cristiani[4,5,6] , Fabio Fontanot[4,6] ,
Manuela Bischetti[4,7] , Angela Bongiorno[3] , Giorgio Calderone[4] , Guido Cupani[4,6] , Valentina D'Odorico[4,6,8] ,
Chiara Feruglio[4,6] , Fabrizio Fiore[4,6] , Francesco Guarneri[4,7,9] , Matteo Porru[4,7] , and Ivano Saccheo[3,10]

[1] INAF–Osservatorio Astronomico di Padova, Vicolo dell'Osservatorio 5, I-35122, Padova, Italy; andrea.grazian@inaf.it
[2] Las Campanas Observatory, Carnegie Observatories, Colina El Pino, Casilla 601, La Serena, Chile
[3] INAF–Osservatorio Astronomico di Roma, Via Frascati 33, I-00078, Monte Porzio Catone, Italy
[4] INAF–Osservatorio Astronomico di Trieste, Via G.B. Tiepolo 11, I-34143, Trieste, Italy
[5] National Institute for Nuclear Physics (INFN), Via Valerio 2, I-34127, Trieste, Italy
[6] Institute for Fundamental Physics of the Universe, Via Beirut 2, I-34151, Trieste, Italy
[7] Dipartimento di Fisica, Sezione di Astronomia, Università di Trieste, Via G.B. Tiepolo 11, I-34131, Trieste, Italy
[8] Scuola Normale Superiore, Piazza dei Cavalieri 7, I-56126 Pisa, Italy
[9] European Southern Observatory, Karl-Schwarzschild-Strasse 2, D-85748, Garching bei Munchen, Germany
[10] Dipartimento di Matematica e Fisica, Università Roma Tre, Via della Vasca Navale 84, I-00146, Roma, Italy

Abstract

One of the key open questions in cosmology is the nature of sources that completed cosmological hydrogen reionization at $z \sim 5.2$. High-z primeval galaxies have been long considered the main drivers of reionization, with a minor role played by high-z active galactic nuclei (AGN). However, in order to confirm this scenario, it is fundamental to measure the photoionization rate produced by active SMBHs close to the Epoch of Reionization. Given the pivotal role played by spectroscopically complete observations of high-z QSOs, in this paper we present the first results of the RUBICON (Reionizing the Universe with Bright Cosmological Nuclei) survey. It consists of a color-selected sample of bona fide $z \sim 5$ QSO candidates from the Hyper Suprime-Cam Subaru Strategic Survey. Our QSO candidates have been validated both by photometric redshifts based on spectral energy distribution fitting and by spectroscopic redshifts, confirming that they lie at $4.5 < z_{\rm spec} < 5.2$. A relatively high space density of QSOs ($\Phi \sim 1.4 \times 10^{-8}$ c Mpc^{-3}) is thus confirmed at $z \sim 5$ and $M_{1450} \sim -27$, consistent with a pure density evolution of the AGN luminosity function from $z = 4$ to $z = 5$, with a mild density evolution rate of 0.25 dex. This indicates that AGN could play a nonnegligible role in cosmic reionization. The Rubicon of reionization has been crossed.

1. Introduction

During its first billion years, the Universe underwent a major phase transition for its main baryonic content, the so-called Epoch of Reionization (EoR). The first stars and black holes produced an intense ultraviolet (UV) radiation that gradually ionized the hydrogen atoms in the intergalactic medium (IGM), creating ionized bubbles growing for approximately 1 Gyr, until they fully percolated at $z \leqslant 6$ (e.g., Fan et al. 2006, 2023; Meiksin 2009; Choudhury 2022). A very late and relatively rapid reionization process has been suggested by current observational constraints (e.g., Planck Collaboration et al. 2020), with a tail end extending at $z \sim 5.2$ (e.g., Eilers et al. 2018; Keating et al. 2020; Bosman et al. 2022; Zhu et al. 2022; Jin et al. 2023) and lasting for $\Delta z \leqslant 2.8$ (George et al. 2015; Reichardt et al. 2021).

The cosmological sources responsible for this disruptive event have been sought for a long time, with conflicting opinions in favor of the two principal suspects, i.e., star-forming galaxies (e.g., Finkelstein et al. 2019) and active galactic nuclei (AGN) (e.g., Giallongo et al. 2012, 2015, 2019;

Boutsia et al. 2018; Grazian et al. 2018, 2020, 2022). The mainstream approach to reionization in the extragalactic community has concentrated for more than 20 years on demonstrating that the reionization process started early and extended in a relatively large redshift interval ($9 < z < 20$), and that it is driven only by faint star-forming galaxies (e.g., Bouwens et al. 2003, 2007; Lehnert & Bremer 2003; Dayal & Ferrara 2018; Trebitsch et al. 2021). This was motivated by early results from the Wilkinson Microwave Anisotropy Probe (Spergel et al. 2003). This scenario, however, has been shown to be in clear contrast with recent measurements of the ionization status of the IGM. The temporal evolution of the neutral hydrogen fraction $x_{\rm HI}$ indicates indeed that it rapidly drops from a value of 1.0 (fully neutral) to a value of $\sim 10^{-4}$ (almost completely ionized) between $z \sim 7$ and $z \sim 5$ (Fan et al. 2006; Hoag et al. 2019; Planck Collaboration et al. 2020; Fontanot et al. 2023). Models assuming relatively faint star-forming galaxies to be the only contributors to the photon budget of the H I ionizing background are thus in tension with the observed rapid and late reionization process, since these galaxies tend to start the reionization process too early (e.g., Naidu et al. 2020).

One of the first astonishing and transformational results of the James Webb Space Telescope (JWST) is that the space density of galaxies at redshift greater than 10 seems to be quite

high, possibly similar to or even higher than the one at redshift 7 (e.g., Labbé et al. 2023; Yan et al. 2023), and therefore it is significantly higher than predictions by numerical simulations (e.g., Haslbauer et al. 2022). It is worth mentioning, however, that these observational results have been based on the very early data from JWST, which could have been affected by (still unknown) calibration issues, e.g., in data reduction, photometric calibration, or astrometry, as discussed in Finkelstein et al. (2022) and Griggio et al. (2023). For example, several galaxies fitted at $z_{phot} > 10$ can be instead extremely dusty starbursts at $z < 5$, as shown by Rodighiero et al. (2023) with the JWST NIRCam survey in SMACS 0723. A more detailed and mature analysis of the first JWST data is certainly needed in the future, corroborated also by spectroscopic confirmations (e.g., Keller et al. 2023). There are two possible explanations to reconcile the high space density of galaxies at $z > 10$ with a scenario of late reionization: either most of these galaxies are at $z < 10$ or very few ionizing photons are able to escape from these high-z galaxies into the IGM.

Lastly, a population of numerous faint high-z AGN candidates has recently emerged from deep JWST spectra (e.g., Brinchmann 2023; Wang et al. 2022; Harikane et al. 2023; Kocevski et al. 2023; Larson et al. 2023; Maiolino et al. 2023; Trump et al. 2023), from compact morphology (Ono et al. 2023), and from deep MIRI photometry (Iani et al. 2022). Recent JWST results from JADES (Robertson et al. 2023) seem to indicate that faint AGN at $z > 4$ are started to be found in deep NIRSpec spectra of normal star-forming galaxies. For example, Übler et al. (2023) and E. Parlanti et al. (in preparation) have found evidence of broad components (FWHM of ~ 2000 km s^{-1}) for Balmer emission lines (e.g., Hα, Hβ) for galaxies at $M_{1500} > -22$ at $z > 4$, e.g., GDS 273 and GDS 3073 in the CANDELS GOODS-South field. These powerful outflows can be powered only by AGN, as shown by Fiore et al. (2023). These two sources have already been shown to host confirmed AGN in the past (Giallongo et al. 2019; Grazian et al. 2020), thanks to X-ray detection by Chandra for GDS 273 and to the detection of the O VI 1032 line in emission for GDS 3073, as confirmed also by Barchiesi et al. (2023). Another result from deep NIRSpec observations is that high-z AGN are quite common at the center of star-forming galaxies, hinting at a high space density of relatively faint accreting SMBHs in the primordial Universe, as recently found in CEERS (Harikane et al. 2023; Kocevski et al. 2023). This result can also have deep implications for the early SMBH seeding/collapse scenario, as recently discussed by Trinca et al. (2022, 2023), Onoue et al. (2023), and Fontanot et al. (2023).

The hypothesis of a high space density of faint AGN at $z > 4$ and their possible contribution to hydrogen reionization is not a new idea. In the last 10 years, indeed, there has been a rising consciousness of the role of AGN as relevant sources of ionizing photons, triggered by several studies focusing on the faint end of the AGN luminosity function at $z \sim 4$–6. The observations of Giallongo et al. (2012, 2015, 2019), Boutsia et al. (2018, 2021), and Grazian et al. (2020, 2022) have hinted at a higher than expected number density of faint AGN at $z \geqslant 4$, which could imply a significant (if not dominant) contribution of AGN to the ionizing UV background, if such number densities hold up to higher redshifts (e.g., Mitra et al. 2018; Fontanot et al. 2023). This scenario has been heavily debated in the past few years, with other studies finding lower AGN

number densities at $z \sim 5$–6 (e.g., Akiyama et al. 2018; McGreer et al. 2018; Parsa et al. 2018; Kulkarni et al. 2019; Niida et al. 2020; Kim & Im 2021; Jiang et al. 2022; Shin et al. 2022; Schindler et al. 2023). These contradicting conclusions on the space density of high-z AGN are likely connected with known problems in candidate selection, based either on deep pencil-beam surveys (highly affected by strong cosmic variance effects) or on shallow wide-area surveys carried out with efficient criteria, but typically affected by large incompleteness.

In this paper we exploit the unique combination of deep and wide areal coverage of the Hyper Suprime-Cam surveys, together with a selection strategy aiming at maximizing selection completeness, in order to place a robust measurement of the space density of $L \sim L^*$ QSOs at $z \sim 5$, close to the main epoch of hydrogen reionization.

The structure of this paper is as follows: In Section 2 we describe a new QSO survey. In Section 3 we address the problematic selection of $z \sim 5$ QSOs and present the first results of a follow-up spectroscopic program. In Section 4 we make a completeness estimate and derive the QSO luminosity function at $M_{1450} \sim -26.5$, discussing the evolution of the QSO space density with redshift, and the derivation of the photoionization rate produced by QSOs at $z \sim 5$. In this section we also check the validity of recent results on the AGN luminosity function at $z > 5$ with a Monte Carlo simulation. We discuss the reliability of these results in Section 5, providing concluding remarks in Section 6. Throughout the paper, we adopt $H_0 = 70$ km s^{-1} Mpc^{-1}, $\Omega_M = 0.3$, and $\Omega_\Lambda = 0.7$, in agreement with the Lambda cold dark matter (ΛCDM) concordance cosmological model. All magnitudes are in the AB photometric system.

2. Data

The RUBICON (Reionizing the Universe with Bright Cosmological Nuclei) survey is an attempt to provide robust constraints to the number density of $L \sim L^*$ QSOs close to the EoR, i.e., at $z \sim 5$. The main aim of the RUBICON survey is to measure the luminosity function of $z \sim 5$ QSOs, to derive their contribution to the photoionization rate measured at high z, and to make preparations for future wide and deep surveys, e.g., with Euclid, the Roman Space Telescope, and the Vera Rubin Legacy Survey of Space and Time (LSST).

Due to the dearth of high-z QSOs, especially at bright magnitudes, large areas of the sky are required in order to build an efficient and statistically meaningful sample of the rare $z \sim 5$ QSOs. Moreover, at these redshifts even the brightest QSOs ($M_{1450} \leqslant -27$) start to appear relatively faint, due to the cosmological dimming effect and to strong IGM absorption (e.g., Inoue et al. 2014). For this reason, we adopt as starting database the Third Public Data Release of the Hyper Suprime-Cam Subaru Strategic Program (HSC-SSP PDR3; Aihara et al. 2022) in order to search for $z \sim 5$ QSOs at $M_{1450} \sim -27$. The HSC-SSP PDR3 survey covers an effective area of 34.7 deg^2 down to magnitudes ~ 25–27 AB in the $grizY$ bands (Deep and Ultradeep surveys, hereafter HSC-Udeep), and a larger area of ~ 1200 deg^2 in three extended regions down to slightly shallower limits of ~ 24–26 AB magnitudes (HSC-Wide survey).

The HSC-Udeep survey allows a unique combination of extended (34.7 deg^2) and deep ($G \sim 27$ mag depth at 5σ) multiwavelength ($grizY$) imaging, which is fundamental to overcoming critical issues related to previous surveys (i.e., large cosmic variance effects in small deep surveys and/or

Table 1
The Bright (Confirmed and Candidate) QSOs at $4.5 \leqslant z \leqslant 5.2$ in the HSC-Udeep Survey

ID	R.A.	Decl.	$magZ_{hsc}$	z_{spec}	Class	z_{phot}	Reference z_{spec}	M_{1450}
2480	34.685304	−4.806873	19.545	4.573	QSO	3.78	SDSS DR17	−26.63
42780	35.302588	−3.714523	19.496	5.011	QSO	4.98	SDSS DR17	−26.89
157404	151.161764	2.209315	19.823	5.007	QSO	4.97	Le Fèvre et al. (2013)	−26.56
258	244.195589	54.324056	19.669	...	Candidate	3.78	...	...
20375	35.334481	−5.390547	18.525	...	Candidate	0.29	...	...
131889	148.729614	1.853699	19.940	...	Candidate	3.42	...	...
213732	244.192594	54.342625	19.842	...	Candidate	1.49	...	...
233735	243.709363	56.147401	19.739	...	Candidate	3.80	...	...

Notes. All these objects are selected through the $G - R$ vs. $I - Z$ color–color criterion. The QSO ID = 42780 has also been reported by McGreer et al. (2018).

large incompleteness in wide but shallow surveys). The HSC-Udeep survey is unique at the present time since it is able to significantly widen the survey discovery space in terms of both magnitude depth and areal coverage. In particular, the HSC-Udeep survey consists of four separate extragalactic fields (SXDS, COSMOS, DEEP2-3, and ELAIS-N1), which allow us to beat down cosmic variance errors to less than 10%, i.e., a negligible value[11] with respect to the Poissonian noise (∼30%–40%), which is assumed to dominate in this survey, given the expected low number of high-z QSOs.

In order to complement the HSC-Udeep survey with larger but shallower areas, with the aim of further reducing cosmic variance effects, we select a 108 deg^2 patch of the HSC-Wide survey, centered around the SXDS field (Furusawa et al. 2008). The selected area covers an extended sky region with R.A. in the interval $29°.0 < $ R.A. $ < 40°.0$ and decl. in the range $-7°.0 < \delta < +3°.0$. The selected sky patch is slightly larger than the area adopted by Niida et al. (2020), allowing us to make further progress in the selection of relatively bright QSOs at $z \sim 5$ and in reducing cosmic variance effects. The HSC-Wide survey is ∼1 mag shallower than the HSC-Udeep survey. This is not a problem for our purposes, since the QSOs we are interested in have apparent magnitudes of ∼20, and the depths of the HSC-Wide database are more than adequate for selecting $z \sim 5$ QSO candidates of $M_{1450} \sim -27$.

3. Selection Method

We select from the HSC-Udeep and HSC-Wide surveys all sources with magnitudes in the z band brighter than $magZ = 20.0$. For each source, we retrieve from the HSC-SSP PDR3 database the point-spread function (PSF) photometry, which is more accurate than Kron magnitudes for pointlike objects. At these apparent magnitudes, indeed, we expect that contamination from extended sources is minimal, and the bulk of sources at $magZ \leqslant 20.0$ are stars or rare QSOs. For the sake of completeness, however, we check that the results in this paper are not affected whether or not the Kron magnitudes are used instead of the PSF photometry.

Spectroscopic redshifts for known QSOs in the HSC-Udeep and HSC-Wide surveys are retrieved from Sloan Digital Sky Survey (SDSS) DR17 (Abdurro'uf et al. 2022) after careful visual inspection of the SDSS spectra, and from SIMBAD[12] and the NASA/IPAC Extragalactic Database.[13] In the HSC-

Udeep area we retrieve from these databases three QSOs with $4.5 < z_{spec} < 5.2$, while in the HSC-Wide region the number of previously known QSOs in this redshift interval is 8. They are shown in the upper part of Tables 1 and 2.

3.1. Selection Criteria in the HSC-Udeep Survey

In the HSC-Udeep area there are 84,122 sources with $magZ \leqslant 20.0$. This is our starting database for high-z QSO selection. We set this relatively bright magnitude limit, $magZ \leqslant 20.0$, for both HSC-Udeep and HSC-Wide, in order to match our catalog with Gaia DR3 (Gaia Collaboration et al. 2023) and exploit this data set to reject stars brighter than $magZ \sim 20$, thanks to the accurate measurements of parallaxes and proper motions still possible at this flux cut. At fainter magnitudes, the Gaia DR3 catalog is less complete and going to fainter magnitudes increases the contamination rate expected from galactic stars. Moreover, we restrict the analysis to an apparent AB magnitude of $magZ \leqslant 20.0$, since we want to study the space density of QSOs close to the luminosity function break ($L \sim L^*$, i.e., $M_{1450} \sim -27$) and to exploit the wide dynamic range in $G - R$ color uniquely afforded by the deep HSC images.

Bona fide QSO candidates at redshift $4.5 < z < 5.2$ are selected with the $G - R$ versus $I - Z$ color selection criterion shown in Figure 1, similar to, but slightly more extended than, the one previously adopted, e.g., by McGreer et al. (2018). The criterion used here ($G - R \geqslant 1.6$, $I - Z \leqslant 0.4(G - R) - 0.3$, and $I - Z \leqslant 0.75$) is able to recover ∼95% of the SDSS DR17 spectroscopically confirmed QSOs in the same redshift interval, indicating the robustness of the adopted color selection. In Figure 1, the known $z \sim 5$ very bright QSOs, discovered by Grazian et al. (2022) in the SkyMapper survey (Wolf et al. 2018), sit inside the adopted color selection criteria, confirming their validity. The synthetic HSC colors of these QSOs are derived through spectral energy distribution (SED) fitting to the observed SkyMapper photometry with AGN libraries fixed at the spectroscopic redshifts of the objects. The gray tracks in Figure 1 are the simulated colors of synthetic QSOs in the redshift range $4.5 < z < 5.2$. The mean IGM absorption by Inoue et al. (2014) is adopted for these tracks. They confirm that the adopted selection criteria are not affected by strong incompleteness.

Among the HSC-Udeep sources brighter than $magZ = 20.0$ and falling in the color–color selection region highlighted in Figure 1, there are four confirmed QSOs, one with spectroscopic redshift $z_{spec} < 4.5$ (big dark-green circle) and three with $4.5 \leqslant z_{spec} \leqslant 5.2$ (big blue circles). There are also five QSO
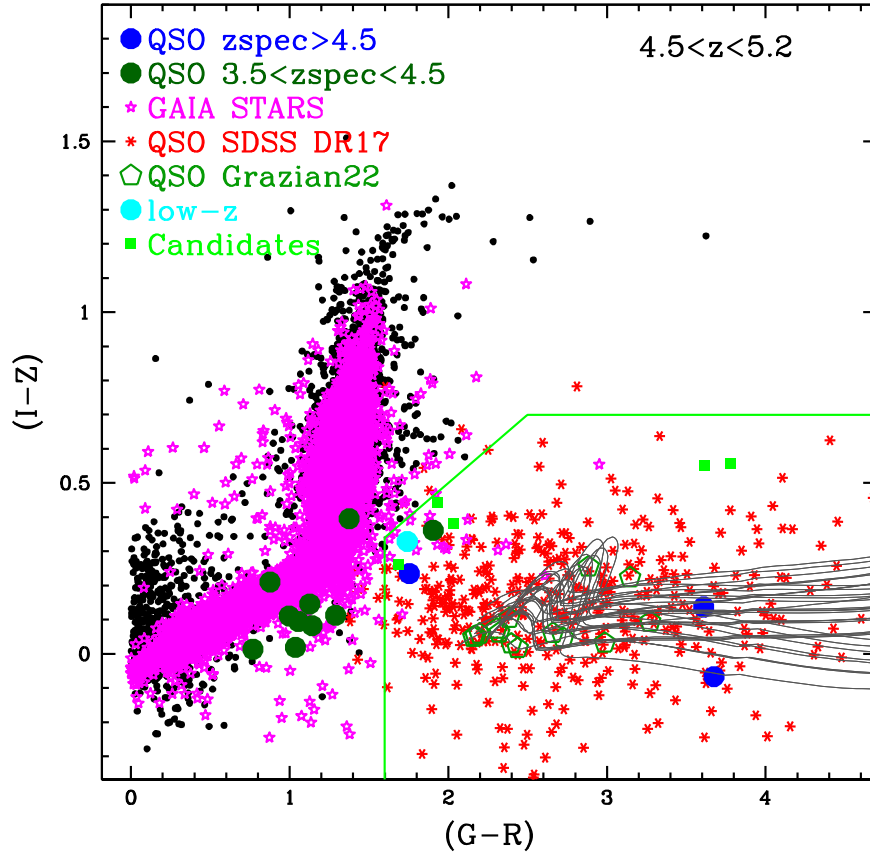
Figure 1. The $G - R$ vs. $I - Z$ color selection criterion for $z \sim 5$ QSO candidates in the HSC-Udeep survey. The black dots are all the objects with magnitude $magZ \leqslant 20.0$, and the red asterisks show the known QSOs with $4.5 \leqslant z_{\mathrm{spec}} \leqslant 5.2$ drawn from SDSS DR17 (Abdurro'uf et al. 2022). The dark-green open pentagons are the known very bright QSOs with $4.5 \leqslant z_{\mathrm{spec}} \leqslant 5.0$ from the QUBRICS survey (Grazian et al. 2022), for which synthetic HSC photometry is derived starting from the observed SkyMapper photometry through SED fitting at their fixed spectroscopic redshift. The big blue circles are the three confirmed QSOs with $4.5 \leqslant z_{\mathrm{spec}} \leqslant 5.2$ in the HSC-Udeep area, while the big dark-green circles indicate known QSOs at $3.5 < z_{\mathrm{spec}} < 4.5$. The cyan circle is a confirmed low-redshift object. The green lines indicate the color criteria for selecting bona fide $z \sim 5$ QSO candidates, while the green squares are the QSO candidates identified in the HSC-Udeep region. Bona fide stars are identified through accurate measurements of parallaxes and proper motions by Gaia DR3 and are marked by magenta stars. The gray tracks are the simulated colors of synthetic QSOs in the redshift range $4.5 < z < 5.2$.

Table 2
The Bright (Confirmed and Candidate) QSOs at $4.5 \leqslant z \leqslant 5.2$ in the HSC-Wide Survey

ID_{Wide}	R.A.	Decl.	$magZ_{\mathrm{hsc}}$	z_{spec}	Classification	z_{phot}	Reference z_{spec}	M_{1450}
45072[a]	34.685307	−4.806874	19.59	4.573	QSO	3.71	SDSS DR17	−26.59
85212[b]	35.302590	−3.714526	19.45	5.011	QSO	4.97	SDSS DR17	−26.94
50470	38.108906	−5.624829	18.55	4.565	QSO	3.75	SDSS DR17	−27.62
155580	32.679849	−0.305117	19.12	4.732	QSO	4.64	McGreer et al. (2013)	−27.13
64891	29.079132	−4.694392	19.18	4.940	QSO	4.79	Wang et al. (2016)	−27.17
124850[c]	30.428719	−1.897370	19.56	5.021	QSO	5.03	This work	−26.83
157472	33.580926	−1.121369	19.92	4.628	QSO	4.57	Alam et al. (2015)	−26.29
220671	29.345417	+2.044333	19.31	4.503	QSO	4.52	Pâris et al. (2014)	−26.83
18331	34.160449	−3.627184	18.77	...	Candidate	3.90	...	...
29348	30.086655	−6.297243	19.83	...	Candidate	1.45	...	...
124908	39.195707	−2.344237	19.75	...	Candidate	3.82	...	...
133691	37.494808	−2.247878	19.62	...	Candidate	3.52	...	...
157609	32.563067	−0.133051	19.94	...	Candidate	3.89	...	...
188088	29.302144	+0.579305	19.81	...	Candidate	3.53	...	...

Notes. All these objects are selected through the $G - R$ vs. $I - Z$ color–color criterion. The eight objects at the top are confirmed QSOs at $z_{\mathrm{spec}} \geqslant 4.5$, while the bottom part of the table includes all the $G - R$ vs. $I - Z$ color-selected QSO candidates.
[a] The same as QSO ID = 2480 in the HSC-Udeep survey.
[b] The same as QSO ID = 42780 in the HSC-Udeep survey.
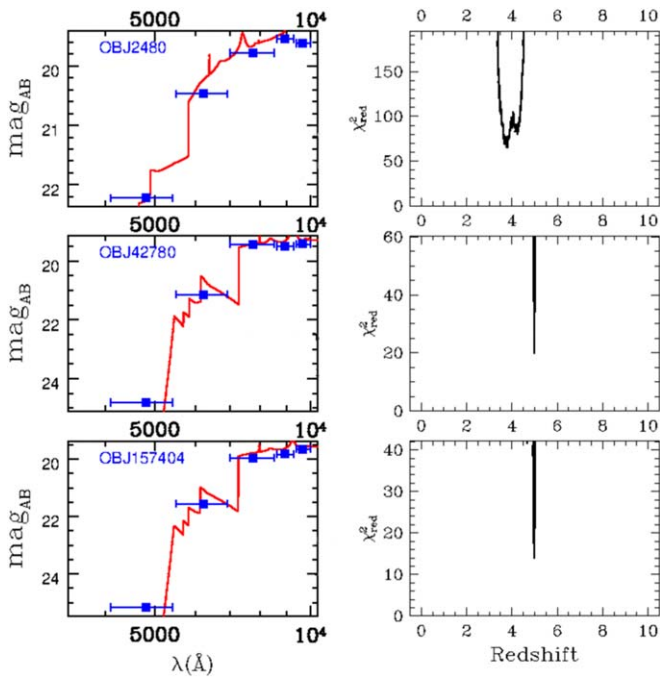[c] Independently discovered by Yang et al. (2023).

Figure 2. The best-fit SED (left) and the $\chi^2(z_{\rm phot})$ at different redshifts (right) for three known QSOs at $z_{\rm spec} \sim 5$ in the HSC-Udeep survey.

candidates with $magZ \leqslant 20.0$ in the color–color selection region highlighted in Figure 1 (small green squares).

For all the known QSOs and candidates selected through the color criteria, we compute the photometric redshifts by adopting a library of synthetic spectra of QSOs taken from the LePhare software (Ilbert et al. 2006), with the mean IGM opacity of Inoue et al. (2014). These photometric redshifts are based on a χ^2 fitting method between the observed photometric catalog and the model SED. The observed photometry, the SED fitting, and the $\chi^2(z_{\rm phot})$ for the three confirmed QSOs at $4.5 \leqslant z_{\rm spec} \leqslant 5.2$ in Table 1 (top) are shown in Figure 2. From Figure 2, it is possible to check that these photometric redshifts give an approximately good indication of the spectroscopic redshifts for the majority of the known QSOs, but for several QSOs, they tend to slightly underestimate the true ones. In particular, a QSO with $z_{\rm spec} \sim 4.6$ has $z_{\rm phot} \sim 3.8$ in Table 1. This is mainly due to the fact that the $G - R$ color is not a strict redshift indicator, but can also be affected by the variance of IGM transmission, which is quite large at $z \sim 5$ (e.g., Inoue et al. 2014; Worseck et al. 2014). The mismatch between photometric redshifts and spectroscopic ones could be due to the fact that the former are computed at a mean IGM absorption (the one by Inoue et al. 2014 in this case), while each high-z QSO has a stochastic IGM absorption along a given line of sight, which is different from that of the others, as discussed, e.g., in Cristiani et al. (2016) and Romano et al. (2019) for QSOs at $z \sim 4$.

The five QSO candidates in the bottom part of Table 1 are shown in Figure A1. The best-fit SEDs of all these candidates show that the $z_{\rm phot}$ for these objects are significantly below 4.5, as summarized in Table 1. Moreover, the absence of a convincing break in the observed $G - R$ color for two of these candidates (ID = 20375 and 213732) could indicate that they possibly are contaminating stars or low-z galaxies, as also indicated by their photometric redshifts. The two candidates at

$z_{\rm phot} \sim 3.8$ (ID = 258 and 233735) could instead be QSOs at $z_{\rm spec} \sim 4.5$, as discussed before for the confirmed QSOs, while object ID = 131889 has $z_{\rm phot} = 3.42$, so it is unlikely that it will turn out to be at $z \geqslant 4.5$.

Despite the large area covered by the HSC-Udeep survey (34.7 deg^2), the number of confirmed QSOs at $4.5 \leqslant z_{\rm spec} \leqslant 5.2$ and $magZ \leqslant 20.0$ is still modest, 3, due to the relatively low value of the QSO space density at high z and bright magnitudes. Two additional candidates could be at $z \sim 4.5$, indicating that the current space density of high-z QSOs provided here is possibly a lower limit.

In order to minimize the cosmic variance effect, we rely also on a larger portion of the sky, observed by the HSC-Wide survey near the SXDS field, as we describe in the following.

3.2. Selection Criteria in the HSC-Wide Survey

In the HSC-Wide region we select 245,946 sources at $magZ \leqslant 20.0$. This is our starting database for high-z QSO selection in the wide area. Figure 3 shows the $G - R$ vs. $I - Z$ color–color diagram for all sources in the HSC-Wide area. The black dots are all the objects with magnitude $magZ \leqslant 20.0$, and the red asterisks show the known QSOs with $4.5 \leqslant z_{\rm spec} \leqslant 5.2$ drawn from SDSS DR17. The dark-green open pentagons are the known very bright QSOs with $4.5 \leqslant z_{\rm spec} \leqslant 5.0$ from the QUBRICS survey (Grazian et al. 2022). The big blue circles are the known QSOs with $4.5 \leqslant z_{\rm spec} \leqslant 5.2$ in the HSC-Wide area. The green lines indicate the adopted color criteria for selecting bona fide $z \sim 5$ QSO candidates, while the green squares are the QSO candidates identified in the HSC-Wide region.

Eight QSOs with $4.5 \leqslant z_{\rm spec} \leqslant 5.2$ are selected by the adopted color criteria, while six candidates at $magZ \leqslant 20.0$ still lack spectroscopic identification, as summarized in Table 2. The photometric redshifts for these objects are derived as described above for the HSC-Udeep sample. The SEDs and χ^2 for these sources are shown in Figures 9, A3, and A4.

As in the case of the HSC-Udeep survey, not all of the QSO candidates in the HSC-Wide area have a photometric redshift above 4.5. One candidate (ID = 29348) has a photometric redshift of $z_{\rm phot} = 1.45$ and its SED is a power law without any evident break, so this is probably a dwarf galaxy at low z, with optical colors similar to those of high-z QSOs. The five remaining candidates have $z_{\rm phot} \geqslant 3.5$, indicating that they are potential QSOs at higher redshifts, given the possible underestimation of the photometric redshift solutions for QSOs, as we find in the HSC-Udeep area. A follow-up spectroscopic confirmation of these candidates is important to derive a complete census of high-z QSOs in this region.

3.3. A Pilot Follow-up Spectroscopic Program in the HSC-Wide Area

In the selected $G - R$ vs. $I - Z$ region of the HSC-Wide survey, we recover seven QSOs at $4.5 < z_{\rm spec} < 5.2$ that were previously known from other spectroscopic surveys in the literature. Another QSO (ID = 124850 at $z_{\rm spec} = 5.021$) has been discovered by a pilot spectroscopic program carried out by our team at the Magellan telescope with IMACS in 2022 November. The spectrum of this new QSO is shown in Figure 4. This object has been independently confirmed by recent spectroscopic follow-up of the QSO candidates in the DESI survey, as described in Yang et al. (2023). This new
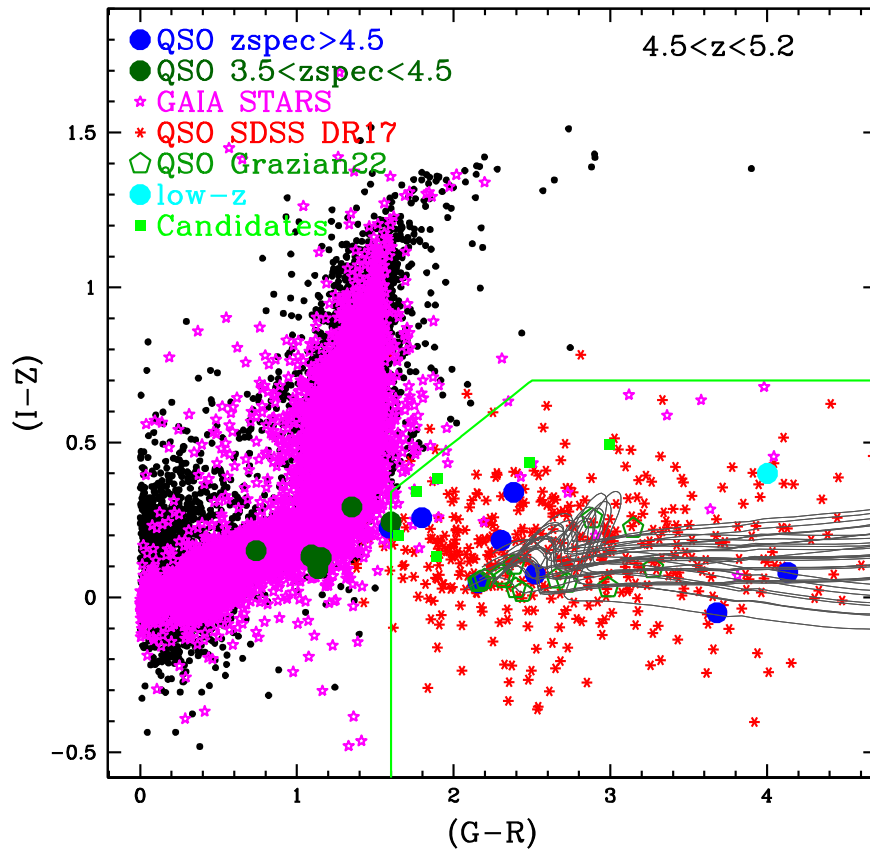
Figure 3. The $G - R$ vs. $I - Z$ color selection criterion for $z \sim 5$ QSO candidates in the HSC-Wide survey. The legend of symbols is the same as that of Figure 1.
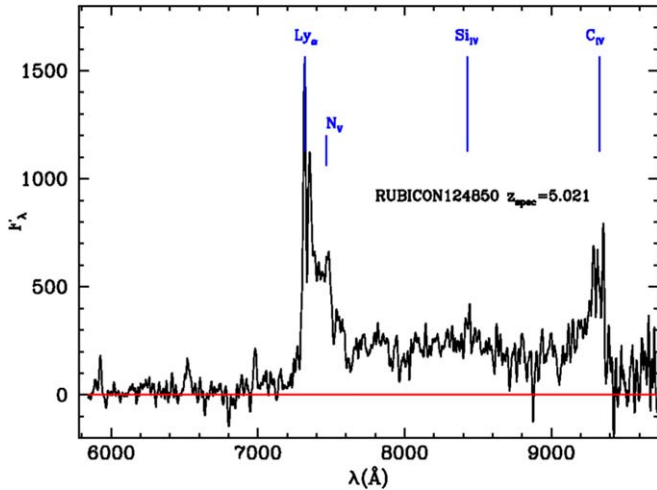

Figure 4. The optical spectrum of the newly discovered QSO ID = 124850 in the HSC-Wide area. This object has been confirmed as a QSO at $z_{\rm spec} = 5.021$, based on the identification of broad Lyα, N V, Si IV, and C IV emission lines. The red line marks the zero level of the continuum.

(The data used to create this figure are available.)

discovery indicates that spectroscopic surveys in this field have not yet completed the identification of relatively bright QSO candidates, and there is still space for improvement, as shown in Table 2.

The number of candidates observed within our pilot spectroscopic project is very limited, and it is not useful at this stage to draw conclusions on the success rate of our color

selection criterion. This will be carried out in the future, once a larger sky area is taken into account. Since the QSO luminosity function is derived by considering only spectroscopically confirmed QSOs, a correct estimate of the success rate of the survey is not needed for the aims of the present paper.

4. Results

4.1. The Completeness of the RUBICON Survey

In order to provide a fair estimate of the completeness of the RUBICON survey, we carry out simulations of synthetic QSO colors. We start from the library of 215 spectra of low-z QSOs from SDSS described in Fontanot et al. (2007) and we convolve each of them with IGM transmission corresponding to 1024 individual lines of sight simulated using the Inoue et al. (2014) formalism, for each redshift bin from $z = 4.0$ to $z = 6.1$ with a separation of $\delta z = 0.1$. The resulting spectra are convolved with the HSC filter curves in $grizY$ to derive the photometry in the HSC bands. The synthetic magnitudes of these $\sim$4.8 million QSOs are perturbed according to the noise statistics of the HSC images, in order to reproduce the observed magnitude–error relation for each filter. In particular, we adopt the magnitude limits at 5σ from Aihara et al. (2022) in order to reproduce the observed trend of magnitudes versus errors for each band. We carry out this exercise for both the HSC-Udeep and HSC-Wide magnitude limits. We then apply the same color criteria shown in Figures 1 and 3 to the synthetic sample affected by noise, and compute the selection function for different apparent magnitudes in the z band (from $magZ = 18.5$ to $magZ = 20.0$) and for different redshifts (from $z = 4.5$ to $z = 5.2$). Figure 5 shows the completeness of the HSC-Udeep
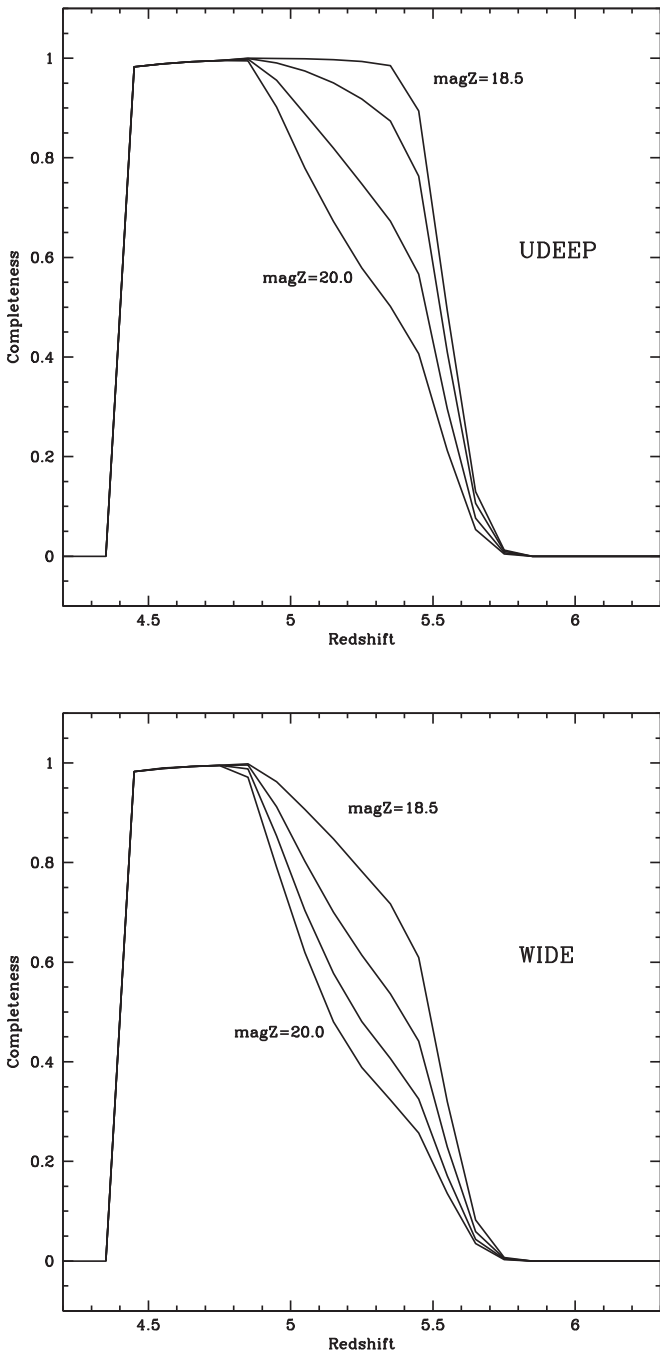
Figure 5. The completeness of the HSC-Udeep and HSC-Wide surveys at different z-band magnitudes (18.5, 19.0, 19.5, and 20.0) as a function of redshift. The completeness is derived through simulations, as described in Section 4.1.

and HSC-Wide surveys derived through these simulations. It turns out that the completeness of the adopted color criteria is almost constant, both in apparent magnitude and in redshift, and the mean value of the completeness is 94% and 88% for the HSC-Udeep and HSC-Wide surveys, respectively.

4.2. The QSO Luminosity Function at $z \sim 5$

The HSC-Udeep sample of confirmed QSOs at $4.5 \leqslant z_{spec} \leqslant 5.2$ in Table 1 is used to compute the luminosity function of $z \sim 5$ QSOs at $M_{1450} \sim -27$. The sample in the HSC-Wide area is used to check the robustness of the results obtained in the relatively small HSC-Udeep area. Indeed, the

larger area adopted here for the HSC-Wide survey allows us to decrease the uncertainties associated with the possibly high cosmic variance in the HSC-Udeep region.

The absolute magnitudes M_{1450} in Tables 1 and 2 are derived for each QSO starting from the observed magnitudes in the z band and the spectroscopic redshifts z_{spec}, taking into account the effect of the distance modulus and the k-correction, as described in Grazian et al. (2022). The luminosity function is computed as the inverse of the accessible volume, summed up for all the confirmed QSOs, as described in detail in Boutsia et al. (2021) and in Grazian et al. (2022). The accessible volume for each individual QSO is corrected for the completeness fraction derived by the simulations described above. In particular, for each QSO we adopt completeness correction as a function of the z-band magnitude and spectroscopic redshift, as shown in Figure 5. Error bars on the space density of QSOs are derived through Poisson statistics, if the number of sources per bin is above 10, or with Gehrels (1986) statistics for smaller numbers. Figure 6 shows the QSO luminosity function at $z \sim 5$. The QSO space density obtained in the HSC-Udeep and HSC-Wide surveys is a factor of ~ 2 higher than the one derived by other surveys in the past (e.g., Yang et al. 2016; McGreer et al. 2018; Kim et al. 2020; Niida et al. 2020; Shin et al. 2020, 2022). The blue continuous line shows the best fit of Boutsia et al. (2021), evolved from $z = 3.9$ to $z \sim 5$ with a redshift evolution of $\gamma = -0.25$, as derived by Grazian et al. (2022), using the results from the QUBRICS survey, which is limited to magnitudes $M_{1450} \leqslant -28.3$. Even in this case, the best fit is a factor of ~ 2–3 larger than the results found by Kulkarni et al. (2019), Giallongo et al. (2019), Grazian et al. (2020), Kim et al. (2020), and Onken et al. (2022). The results we present here for the RUBICON survey are consistent with the parameterization found by Boutsia et al. (2021) and the evolution of the QSO space density derived by Grazian et al. (2022), as shown in Figure 6. This result confirms that the evolution of the QSO luminosity function is consistent with a pure density evolution in the range $3.5 < z < 5.5$, with a relatively shallow declining rate (~ -0.25 dex), as found by Grazian et al. (2022) and Fontanot et al. (2023).

4.3. Maximum Likelihood Simulations

Maximum likelihood probabilities are also computed, adopting as reference a large collection of publicly available parameterizations for the QSO luminosity function at comparable redshifts. We carry out a Monte Carlo simulation in order to predict the expected number of QSOs with $4.5 \leqslant z_{spec} \leqslant 5.2$ and magnitude $Z \leqslant 20.0$ observed in the 34.7 deg^2 HSC-Udeep area and in the 108 deg^2 HSC-Wide survey considered here, according to different parameterizations of the QSO luminosity function proposed at $z \gtrsim 5$. If the adopted luminosity function is not available exactly at $z = 5.0$, we adopt a pure density evolution with the $d\log\Phi/dz$ parameter quoted in each paper. For each best-fit value of a given luminosity function listed in Table 3, we randomly extract the redshifts and absolute magnitudes M_{1450} for the expected QSOs in a given area of the sky. We then assign to each simulated QSO a synthetic SED, randomly taken from the library used to compute the photometric redshifts described in Section 3. The selected SED is then redshifted to the assigned redshift and normalized according to the given absolute magnitude M_{1450}. This spectrum is then convolved with the filters adopted for the
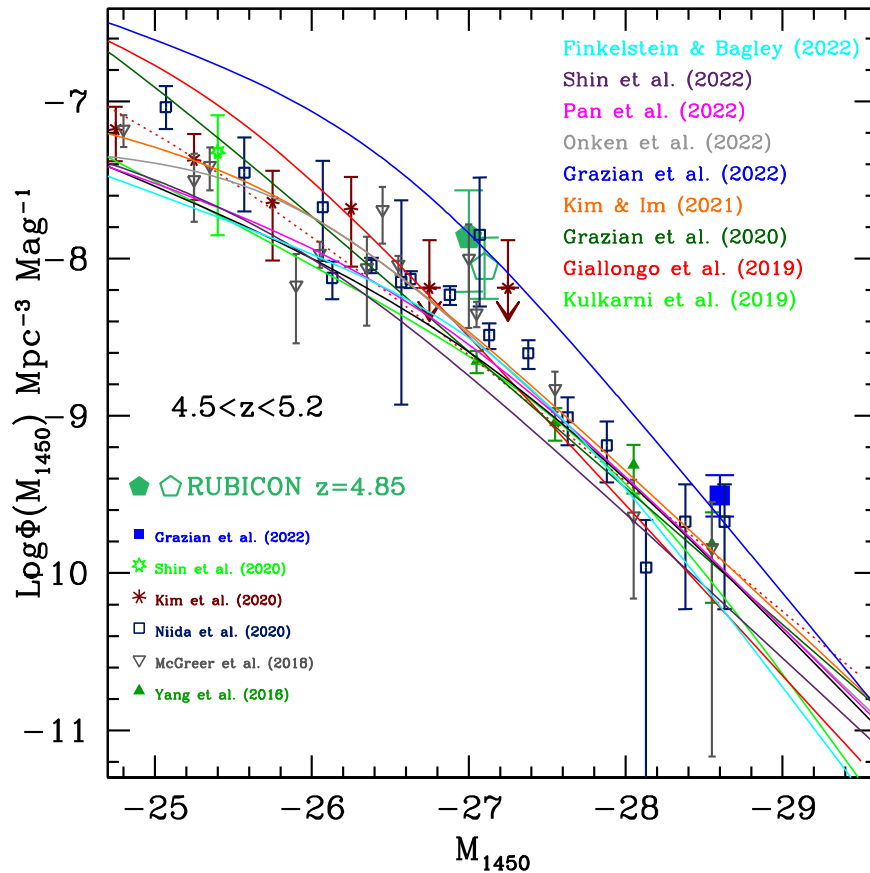
Figure 6. The QSO luminosity function at $z \sim 5$ from the HSC-Udeep and HSC-Wide surveys. The filled green pentagon shows the space density of $z \sim 5$ QSOs in the HSC-Udeep area, while the open green pentagon shows the space density in the HSC-Wide area, considering only confirmed QSOs with available spectroscopic redshifts. These values are a factor of ~ 2–3 larger than previous determinations available in the literature, highlighted by small symbols. The magenta line is model 4 of Pan et al. (2022).

HSC survey and the observed magnitudes in the *grizY* photometric system are derived for each simulated QSO. We do not take into account here the effects of the photometric errors, since at the bright magnitude limit adopted here ($Z \leqslant 20.0$) the photometric uncertainties should be small. We then select all the simulated QSOs within the same redshift and luminosity range of the observed sample, i.e., with $4.5 \leqslant z_{spec} \leqslant 5.2$ and magnitude $Z \leqslant 20.0$. We repeat the simulations for 10^4 iterations. For each parameterization of the QSO luminosity function we then derive the mean number N_{qso} of QSOs expected for the HSC-Udeep and HSC-Wide areas, the standard deviation on N_{qso} for the 10^4 random realizations, and the probability of recovering at least nine objects (i.e., the number of observed QSOs in the HSC-Udeep and HSC-Wide surveys) using the same selection criteria in these 10^4 iterations, which is called Prob($N_{qso} \geqslant 9$). Since the spectroscopic confirmation of the candidates in Tables 1 and 2 is not finished yet, and given also the incompleteness of the RUBICON survey discussed above, the observed number of high-z QSOs can be considered as a lower limit to the real number of $z \geqslant 4.5$ QSOs. For this reason, we measure the likelihood of each luminosity function parameterization by computing Prob($N_{qso} \geqslant 9$).

First of all, we check the consistency of the luminosity function of Grazian et al. (2022) with the observed number of high-z QSOs in the RUBICON survey. According to Table 3, the expected number of QSOs (at $magZ \leqslant 20$ and $4.5 \leqslant z_{spec} \leqslant 5.2$) for the HSC-Udeep and HSC-Wide surveys investigated here

should be $N_{sim} \sim 16$ for the parameterization of Grazian et al. (2022). In the same magnitude and redshift intervals, we observe nine bright QSOs. This does not mean, however, that the Grazian et al. (2022) prediction is overestimated by a factor of ~ 2, since in these simulations we assume a completeness of 100%, while in reality the completeness is of the order of 88%–94%, as we find in this work. Moreover, the spectroscopic identification of the QSO candidates in our area is not finished yet, and other $z > 4.5$ QSOs could be discovered among the targets in Table 1 or Table 2. For example, the candidates ID = 258 and 233735 in HSC-Udeep and ID = 18331, 124908, and 157609 in HSC-Wide have $z_{phot} \sim 3.8$ and all of them could be finally confirmed at $z_{spec} > 4.5$, as we discuss in the previous paragraph.

Table 3 summarizes the expected numbers and the associated probabilities Prob($N_{qso} \geqslant 9$) for a number of QSO luminosity functions that appeared recently in the literature. Only the parameterization of Grazian et al. (2022) has a probability greater than 80% of observing nine or more QSOs in the HSC-Udeep and HSC-Wide surveys, while all the other luminosity functions have a probability less than 20%, due to their much lower normalization in space density. In particular, the parameterizations by Pan et al. (2022) (models 1–3) have probabilities Prob($N_{qso} \geqslant 9$) of $\sim 7\%$–20%, while all the other luminosity functions have probabilities less than $\sim 2\%$. We can thus conclude that all the previous luminosity functions of $z \sim 5$ QSOs are excluded at the 1σ confidence level (corresponding to 16% probability), while only the QSO luminosity functions of Grazian et al. (2022) and model 3 of Pan et al.

Table 3
The Expected Number of QSOs and the Maximum Likelihood of Different QSO Luminosity Functions for the HSC-Udeep and HSC-Wide Surveys

Paper	N_{qso}	rms N_{qso}	Prob($N_{qso} \geqslant 9$)
Grazian et al. (2022)	16.02	3.99	98.03%
Harikane et al. (2023)	0.05	0.07	0.00%
Matsuoka et al. (2023)	0.06	0.25	0.00%
Schindler et al. (2023)	0.29	0.55	0.00%
Shin et al. (2022) w/o K20	2.10	1.47	0.00%
Shin et al. (2022) w/ K20	2.11	1.44	0.00%
Jiang et al. (2022) model 75% c.l.	0.12	0.36	0.00%
Jiang et al. (2022) model 95% c.l.	0.14	0.39	0.00%
Onken et al. (2022) w/ Kim20	3.59	1.89	1.39%
Onken et al. (2022) w/ Niida20	2.69	1.61	0.14%
Pan et al. (2022) model 1	4.98	2.24	7.26%
Pan et al. (2022) model 2	5.49	2.30	9.83%
Pan et al. (2022) model 3	6.45	2.57	19.68%
Pan et al. (2022) model 4	2.58	1.54	0.08%
Finkelstein & Bagley (2022)	3.23	1.72	0.31%
Kim & Im (2021) case 1	2.50	1.55	0.06%
Kim & Im (2021) case 2	3.01	1.73	0.42%
Kim & Im (2021) case 3	3.46	1.87	0.11%
Kim et al. (2020) model 1	2.71	1.65	0.28%
Kim et al. (2020) model 1b	2.42	1.57	0.00%
Kim et al. (2020) model 1c	2.43	1.59	0.21%
Kim et al. (2020) model 2	2.89	1.73	0.14%
Kim et al. (2020) model 2b	2.51	1.64	0.16%
Kim et al. (2020) model 2c	3.31	1.78	0.52%
Niida et al. (2020) w/ ML, fixed β	3.39	1.86	0.68%
Niida et al. (2020) w/ χ^2, fixed β	2.97	1.74	0.28%
Niida et al. (2020) w/ ML, free β	3.53	1.82	0.74%
Kulkarni et al. (2019) model 1	2.23	1.36	0.04%
Kulkarni et al. (2019) model 2	1.46	1.09	0.00%
Kulkarni et al. (2019) model 3	1.33	1.00	0.00%
McGreer et al. (2018) w/ DPL	1.19	1.08	0.00%
McGreer et al. (2018) w/ paper I	0.87	0.91	0.00%
Yang et al. (2016) model 1	0.74	0.85	0.00%
Yang et al. (2016) model 2	0.75	0.86	0.00%
Yang et al. (2016) model 3	0.69	0.85	0.00%
Yang et al. (2016) model 4	0.80	0.88	0.00%

Note. Results of 10^4 simulations.

(2022) are consistent with the present data at more than 1σ. Adopting a more stringent threshold of 2.3% confidence level, corresponding to 2σ, the luminosity functions of the following papers are not (statistically) acceptable: Yang et al. (2016), McGreer et al. (2018), Kulkarni et al. (2019), Niida et al. (2020), Kim et al. (2020), Kim & Im (2021), Finkelstein & Bagley (2022), Onken et al. (2022), Jiang et al. (2022), Shin et al. (2022), Schindler et al. (2023), Harikane et al. (2023), Matsuoka et al. (2023), and model 4 of Pan et al.(2022).

4.4. The Photoionization Rate Produced by z ∼ 5 AGN

A recent estimate of the H I photoionization rate produced by $z \sim 4$ AGN has been provided by Boutsia et al. (2021). The crucial ingredient in this analysis is the robust determination of the shape and normalization of the AGN luminosity function in an extended ($-30 < M_{1450} < -18$) luminosity range, thanks to the combination of wide surveys (e.g., QUBRICS; Calderone et al. 2019; Boutsia et al. 2020; Guarneri et al. 2021) with deep observations (Fontanot et al. 2007; Glikman et al. 2011; Boutsia et al. 2018; Giallongo et al. 2019). Based on this result, Boutsia et al. (2021) concluded that AGN are able to produce

∼100% of the H I ionizing photons at $z \sim 4$, measured through Lyman forest fitting or via the proximity effect, if the escape fraction of ∼75% measured for bright QSOs (Cristiani et al. 2016; Romano et al. 2019) is a common feature also for fainter sources around and below the knee of the AGN luminosity function (Grazian et al. 2018).

In our previous work (Grazian et al. 2022), we found that the space density of $M_{1450} \sim -28.5$ QSOs at $z \sim 5$ is 3 times higher than previous determinations, confirming the recently derived results by Onken et al. (2022) at $z \gtrsim 4.5$ and by Schindler et al. (2019a, 2019b) and Boutsia et al. (2021) at $z \sim 3-4$. In Grazian et al. (2022) we also found that the density evolution of the AGN luminosity function from $z = 4$ to $z = 5$ is milder than previously reported determinations, e.g., from SDSS, and that the $z \sim 5$ AGN luminosity function shows the same shape of the $z \sim 4$ one, with a slightly lower normalization, by ∼0.25 dex. Recent results by CEERS seem to confirm this picture, indicating that the space density of $z \sim 5$ AGN is relatively high at $M_{1450} \sim -19.5$ (Harikane et al. 2023; Kocevski et al. 2023), confirming early determinations by Giallongo et al. (2019) and Grazian et al. (2020). In practice, the QSO luminosity function seems to follow a pure density evolution with a mild rate.

The results of this paper confirm the achievements of Grazian et al. (2022) at slightly fainter luminosities, $M_{1450} \sim -27$, close to the knee of the luminosity function, where the space density of $z \sim 5$ QSOs is still 2–3 times higher than that of previous surveys. We assume here that the mean free path of H I ionizing photons is 17.4 proper Mpc at $z = 4.75$ (Worseck et al. 2014) and that the Lyman continuum (LyC) escape fraction of $z \sim 5$ QSOs is $\gtrsim 70\%$, similar to the one measured at $z \sim 4$ by Cristiani et al. (2016), Grazian et al. (2018), and Romano et al. (2019). It is then possible to compute the contribution of $z \sim 5$ QSOs to the H I photoionization rate, by integrating the extrapolated luminosity function in the interval $-30 \leqslant M_{1450} \leqslant -18$. Figure 7 shows the photoionization rate produced by $z \sim 5$ QSOs, according to the luminosity function provided in Grazian et al. (2022), which is consistent with the data found in this work. It turns out that bright QSOs and faint AGN can account for ∼50%–100% of the required photon budget[14] to explain the observed ionizing background measured close to the end of the EoR, as also shown by Grazian et al. (2022) and Fontanot et al. (2023). The photoionization rate of AGN derived here, $\Gamma_{-12} = 0.456\,\mathrm{s}^{-1}$, is consistent with the recent estimate at $z \sim 5$ of Gaikwad et al. (2023), possibly indicating that bright QSOs and faint AGN together are able to provide ∼100% of the ionizing background of the IGM. This may suggest that QSOs and AGN can play an important role in the cosmological reionization process of hydrogen.

5. Discussion

5.1. Comparison with Recent Surveys of z ∼ 5 QSOs

It is worth asking why recent surveys of $z \sim 5$ bright QSOs, e.g., Niida et al. (2020) and Shin et al. (2022), found a QSO number density that is significantly lower than our values. In

---

[14] This uncertainty is due to the factor of 2 scatter in the measurement of the hydrogen photoionization rate measured through Lyman forest fitting (Bolton & Haehnelt 2007; Wyithe & Bolton 2011; Becker & Bolton 2013; Davies et al. 2018; Faucher-Giguère 2020; Gallego et al. 2021; Gaikwad et al. 2023) or with the proximity effect (Calverley et al. 2011), as discussed in Boutsia et al. (2021) and Grazian et al. (2022).
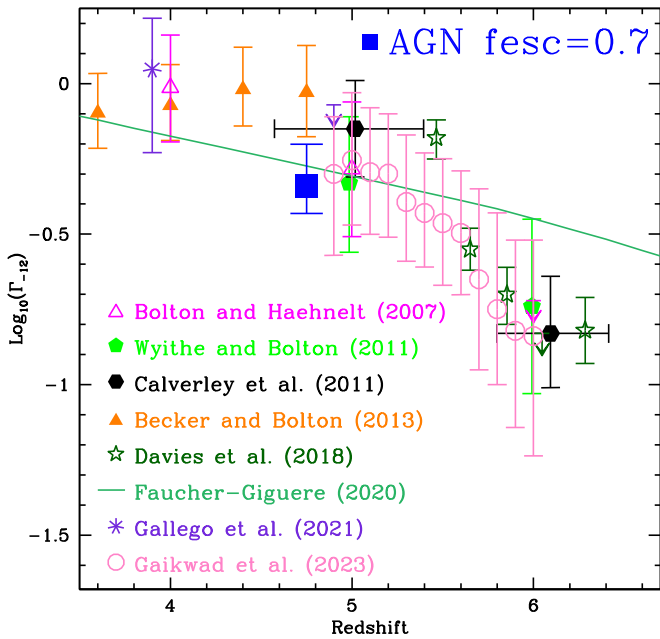
Figure 7. The photoionization rate of the IGM measured by Lyman forest fitting (Bolton & Haehnelt 2007; Wyithe & Bolton 2011; Becker & Bolton 2013; Davies et al. 2018; Faucher-Giguère 2020; Gallego et al. 2021; Gaikwad et al. 2023) and with the proximity effect (Calverley et al. 2011). The ionizing background produced by bright QSOs and faint AGN at $z \sim 5$ is shown by the blue square, assuming a LyC escape fraction of 70%.

order to carry out a fair comparison, we carefully check the criteria adopted by these two surveys.

Starting from Niida et al. (2020), we check that our QSO ID = 157404 in the HSC-Udeep survey (see Table 1) is outside their area. The other two QSOs at $z > 4.5$ in our HSC-Udeep survey, in contrast, are part of the area covered by Niida et al. (2020). The first object, ID = 2480, does not satisfy their $R - I$ color criterion, i.e., $R - I > 1.0$. Object ID = 42780 in Table 1 satisfies all their color criteria and it is plausibly included in the Niida et al. (2020) QSO sample (their parent QSO sample is not publicly available). From this comparison, we can conclude that the QSO luminosity function of Niida et al. (2020) could be 50% incomplete at $M_{1450} \sim -27$, and by applying this correction factor, their QSO space density turns out to be compatible with our results in Figure 6.

In order to compare our results with those of Shin et al. (2022), we download the full HSC-Udeep survey from the HSC PDR2 repository. QSO ID = 157404 in Table 1 is outside their area, while the other two $z \geqslant 4.5$ QSOs, ID = 2480 and ID = 42780, have been recovered by PDR2. It is difficult to reproduce the selection criteria of Shin et al. (2022), but it is clear that these two objects are missing from their final sample. We can thus conclude that their incompleteness could be substantial at $M_{1450} \sim -27$. It is thus not surprising at all that they found a much lower QSO number density than our results in Figure 6.

The reason why previous surveys found a low number density of $z > 4.5$ QSOs could be their incompleteness. Out of the eight known QSOs at $z > 4.5$ in the HSC-Wide survey (Table 2), only three have been discovered by SDSS, while the other QSOs have been found by different surveys. Thus, the total number of $z > 4.5$ QSOs is large in the considered area, but individual surveys in the past only recovered a small fraction of them, possibly due to their efficient but strict

selection criteria, which lost a nonnegligible fraction of high-z objects. As an example, if we adopted only a subsample of the color criteria by McGreer et al. (2018), i.e., $G - R \geqslant 1.8$ and $I - Z \leqslant 0.5$, we would select only two of the three QSOs at $z_{spec} \geqslant 4.5$ in the HSC-Udeep survey and only six of the eight QSOs at $z_{spec} \geqslant 4.5$ in the HSC-Wide area, a further reduction of 66%–75% of the survey completeness. If we applied all the color criteria of McGreer et al. (2018), i.e., $G - R \geqslant 1.8$, $I - Z \leqslant 0.5$, $R - I \geqslant 1.3$, $I - Z \leqslant 0.15 + 0.875 \times (R - I - 1.30)$, we would select only two of the three QSOs at $z_{spec} \geqslant 4.5$ in the HSC-Udeep survey and only three of the eight QSOs at $z_{spec} \geqslant 4.5$ in the HSC-Wide area. In this case, by applying the more stringent color criteria by McGreer et al. (2018), the completeness drops to a level of 38%–66%.

As a general comment, surveys searching for high-z QSOs are usually very efficient, above 50% (e.g., Shin et al. 2022), but their completeness level could be very low, as already pointed out in Grazian et al. (2020), Boutsia et al. (2021), and this paper. This incompleteness is even more exacerbated in the case of shallow surveys, where the photometric scatter, especially in the bands used for dropout, could undermine the completeness of the selection criteria adopted. It is thus not surprising at all that in the past there were a number of claims of a low space density of high-z QSOs (e.g., Yang et al. 2016; McGreer et al. 2018; Kulkarni et al. 2019; Kim et al. 2020; Niida et al. 2020; Kim & Im 2021; Finkelstein & Bagley 2022; Jiang et al. 2022; Onken et al. 2022; Pan et al. 2022; Shin et al. 2022; Matsuoka et al. 2023; Schindler et al. 2023), which are not supported by the data of this paper. A possible way out to have a high level of completeness, while keeping the efficiency of spectroscopic surveys acceptable, is to adopt selection methods based on machine learning and iterative removal of low-probability candidates (G. Calderone et al., in preparation). It will be interesting in the future to apply this method to the entire HSC database.

5.2. Considerations and Implications from the RUBICON Survey

A number of considerations can be drawn here from the QSO search we have carried out on the HSC-Udeep and HSC-Wide surveys. The relevant points are as follows:

1. The application of a magnitude threshold $magZ \leqslant 20$ to the Gaia database is very efficient in rejecting stars, as shown in Figures 1 and 3.

2. The extended dynamic ranges in the G and R bands of the HSC-Udeep and HSC-Wide surveys are important in selecting high-z QSOs, as shown in Figures 1 and 3.

3. The spread in $G - R$ color is due to both the redshift evolution and fluctuations of the IGM opacity in different lines of sight. Objects with blue $G - R$ colors (~ 1.6) can be at $z \geqslant 4.5$, as shown in Figure 1. In order to compute the completeness level and the selection function, detailed simulations have been carried out by including the stochasticity of the IGM absorption at these redshifts.

4. The $G - R$ color selection could be biased toward QSOs with low mean free paths or negligible escape fractions of LyC photons. A possible solution to this issue is to carry out extensive spectroscopic confirmation of candidates that lie close to the border of the color selection region, outside the adopted criteria. The selection of objects with $G - R \leqslant 1.6$ will allow us to quantify the completeness

of our color criteria and the effective distribution of the mean free path of ionizing photons. This will be possible thanks to the availability of parallaxes and proper motions of unprecedented quality from Gaia, which allows us to clean the catalog of contaminating stars.

5. Photometric redshifts tend in a few cases to underestimate the spectroscopic redshifts of QSOs, as shown by the spectroscopically confirmed QSOs in Table 1 and Table 2. For this reason, the spectroscopic follow-up should be extended to objects with $3.7 \leqslant z_{phot} \leqslant 4.5$ in the future.

6. Photometric redshifts are computed at the mean IGM transmission of Inoue et al. (2014). At high redshift, a large scatter of the IGM absorption τ_{IGM} is expected. Detailed simulations of the IGM variance have been carried out in order to calculate the effective completeness of the RUBICON survey.

The lesson learned from the RUBICON survey is that the number of interlopers is relatively low in the color selection region adopted (provided that relatively deep surveys are available), and the HSC-Wide and HSC-Udeep data are very promising for addressing the key question of the space density of $\sim L^*$ AGN at $z \sim 5$. The results shown in Figure 6 and Table 3 are based only on the spectroscopically confirmed QSO sample. In the future, the spectroscopic confirmation of all the candidates in Tables 1 and 2 will be important for assessing the completeness of these surveys.

6. Conclusions

In this paper we present the first results of the RUBICON survey, aimed at constraining the space density of relatively bright QSOs ($M_{1450} \sim -27$) at $z \sim 5$, i.e., at the end of the reionization epoch (Eilers et al. 2018; Keating et al. 2020; Bosman et al. 2022; Zhu et al. 2022).

From the ultradeep imaging in the *grizY* bands covering 34.7 deg^2 in the HSC-Udeep survey (Aihara et al. 2022), an almost complete sample of three spectroscopically confirmed QSOs at $4.5 < z < 5.2$ and $magZ \leqslant 20.0$ is drawn (see Figure 1 and Table 1). QSO candidates at $z \sim 5$ are selected through the $G - R$ vs. $I - Z$ color–color criteria, as shown in Figure 1. Bona fide stars are excluded, based on parallax and proper-motion information from Gaia DR3 (Gaia Collaboration et al. 2023). Two promising candidates in HSC-Udeep have $z_{phot} \sim 3.8$, and they can also be at $z_{spec} > 4.5$, due to the tendency of our photo-z to underestimate the spectroscopic redshifts of high-z QSOs (see Table 1). Spectroscopic confirmation of these targets is currently ongoing.

In order to check the reliability of our results on even larger areas, the HSC-Udeep survey is complemented by adding 108 deg^2 of wide and deep imaging in the HSC-Wide area, finding eight spectroscopically confirmed QSOs (two are in common with the HSC-Udeep survey) and five QSO candidates at $magZ \leqslant 20.0$ with redshift $z_{phot} \geqslant 3.5$ (see Figure 3 and Table 2). Some of these candidates are also expected to be QSOs with $z_{spec} > 4.5$, pending spectroscopic confirmation in the future. One of the known QSOs (ID = 124850) has been confirmed by spectroscopic observations at the Magellan telescope (Las Campanas Observatory) in 2022 November, triggered by the RUBICON survey. This QSO has been independently discovered by Yang et al. (2023).

The HSC-Udeep area is divided into four well-separated fields (SXDS, COSMOS, DEEP2-3, and ELAIS-N1), thus minimizing cosmic variance effects ($\sim 10\%$). For comparison, the Poissonian error in the same corresponding area is $\sim 30\%$–40%, thus dominating the uncertainty of this survey, due to the expected low number of high-z QSOs.

The luminosity function of $z \sim 5$ QSOs (Figure 6) is computed as the inverse of the accessible cosmological volume at $4.5 \leqslant z \leqslant 5.2$, summed up for all the spectroscopically confirmed sources in the HSC-Udeep survey. A completeness of 94% is assumed. The same calculation is carried out in the HSC-Wide survey, giving comparable results in terms of QSO space density. These $z \sim 5$ QSO luminosity functions are ~ 2–3 times larger than the ones derived by Yang et al. (2016), McGreer et al. (2018), Kulkarni et al. (2019), Niida et al. (2020), Kim et al. (2020), Kim & Im (2021), Finkelstein & Bagley (2022), Onken et al. (2022), Jiang et al. (2022), Shin et al. (2022), Schindler et al. (2023), Harikane et al. (2023), Matsuoka et al. (2023), and model 4 of Pan et al. (2022). The maximum likelihood approach summarized in Table 3 confirms the results obtained with nonparametric luminosity function analysis. We estimate the expected number of QSOs from the published parameterizations of the $z \sim 5$ QSO luminosity functions. We show that all of them, with the relevant exception of those of Grazian et al. (2022) and models 1–3 of Pan et al. (2022), predict a too low number of QSOs (and are thus incompatible with our findings at the $>2\sigma$ confidence level).

It is clear, from Figure 6 and from the maximum likelihood analysis in Table 3, that the only viable parameterization of the QSO luminosity function in agreement with the present data is the one of Grazian et al. (2022). This has deep implications for the role of high-z AGN in the H I reionization event. We assume an escape fraction of 70% at all redshifts and luminosities, and we integrate the QSO luminosity function of Grazian et al. (2022) in the interval $-30 \leqslant M_{1450} \leqslant -18$. Given a mean free path of 17.4 proper Mpc at $z = 4.75$, it turns out that AGN are able to produce $\sim 50\%$–100% of the ionizing background at the end of the reionization epoch. In particular, recent claims of a negligible role of AGN in H I reionization, based on earlier luminosity function estimates (e.g., Yang et al. 2016; McGreer et al. 2018; Kulkarni et al. 2019; Kim et al. 2020; Niida et al. 2020; Kim & Im 2021; Finkelstein & Bagley 2022; Jiang et al. 2022; Onken et al. 2022; Pan et al. 2022; Shin et al. 2022; Harikane et al. 2023; Matsuoka et al. 2023; Schindler et al. 2023), are formally excluded at more than the 2σ level, given our results here on the luminosity function of $z \sim 5$ QSOs.

We provide here starting evidence in terms of QSO number density that AGN can produce a substantial amount of the required ionizing photons to sustain the final phases of the reionization epoch at $z \sim 5$. In the future, the RUBICON survey can be extended both in terms of area, within the entire HSC-Wide area (~ 1200 deg^2), and in terms of depth, thanks to the deep imaging already available in the HSC-Udeep survey (e.g., Desprez et al. 2023). If confirmed by future studies, this will have a strong impact on the study of reionization and on the sources responsible for this cosmological event.

It is now time to cross the Rubicon of reionization with QSOs: "alea iacta est" (Caesar, 49 B.C.).

Appendix
The SEDs of Confirmed and Candidate QSOs

Examples of SEDs are presented for QSO candidates in the HSC-Udeep survey (Figure A1) and for confirmed QSOs and QSO candidates in the HSC-Wide area (Figures A2, A3, and A4).
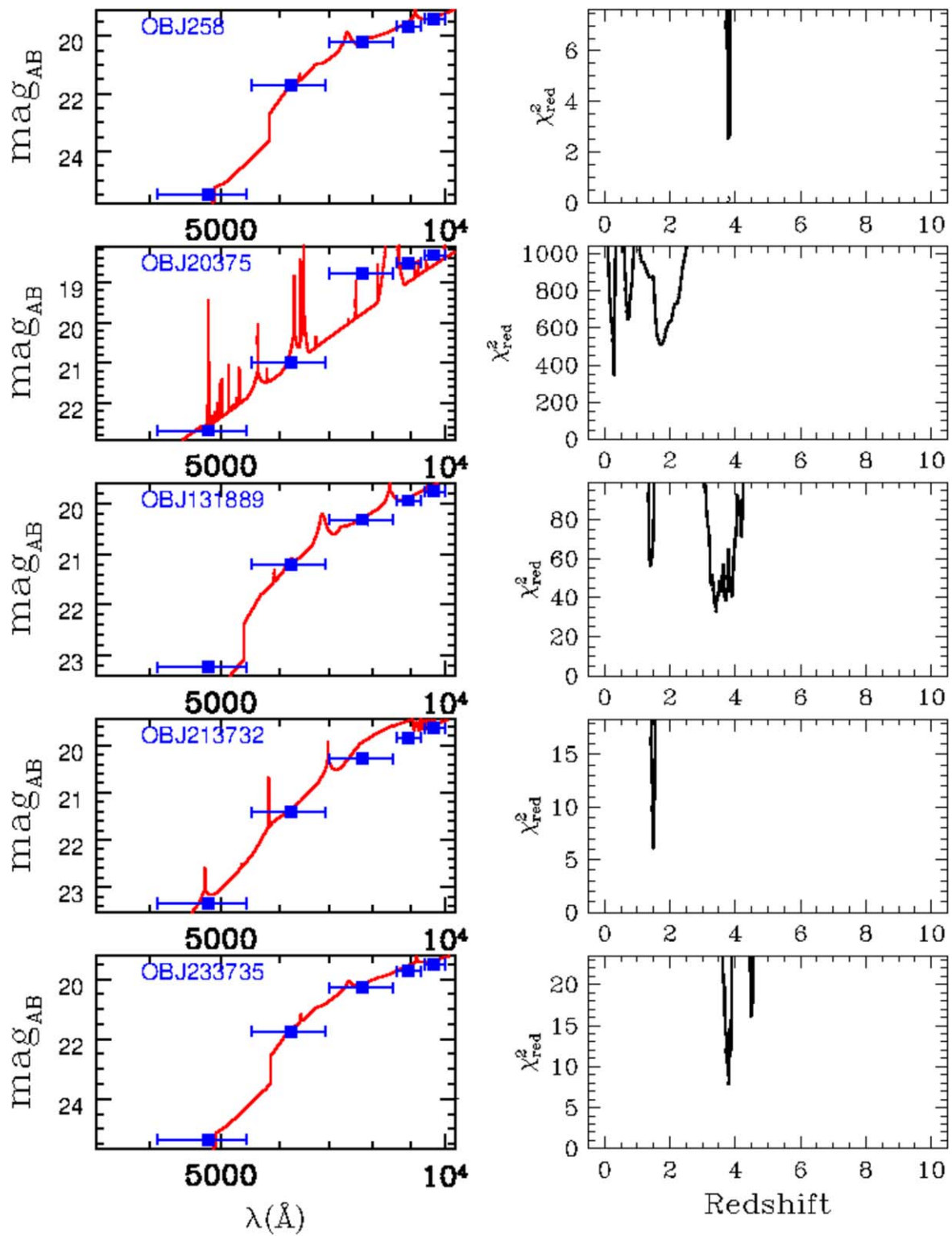
Figure A1. The best-fit SED (left) and the $\chi^2(z_{phot})$ at different redshifts (right) for color-selected QSO candidates in the HSC-Udeep survey.
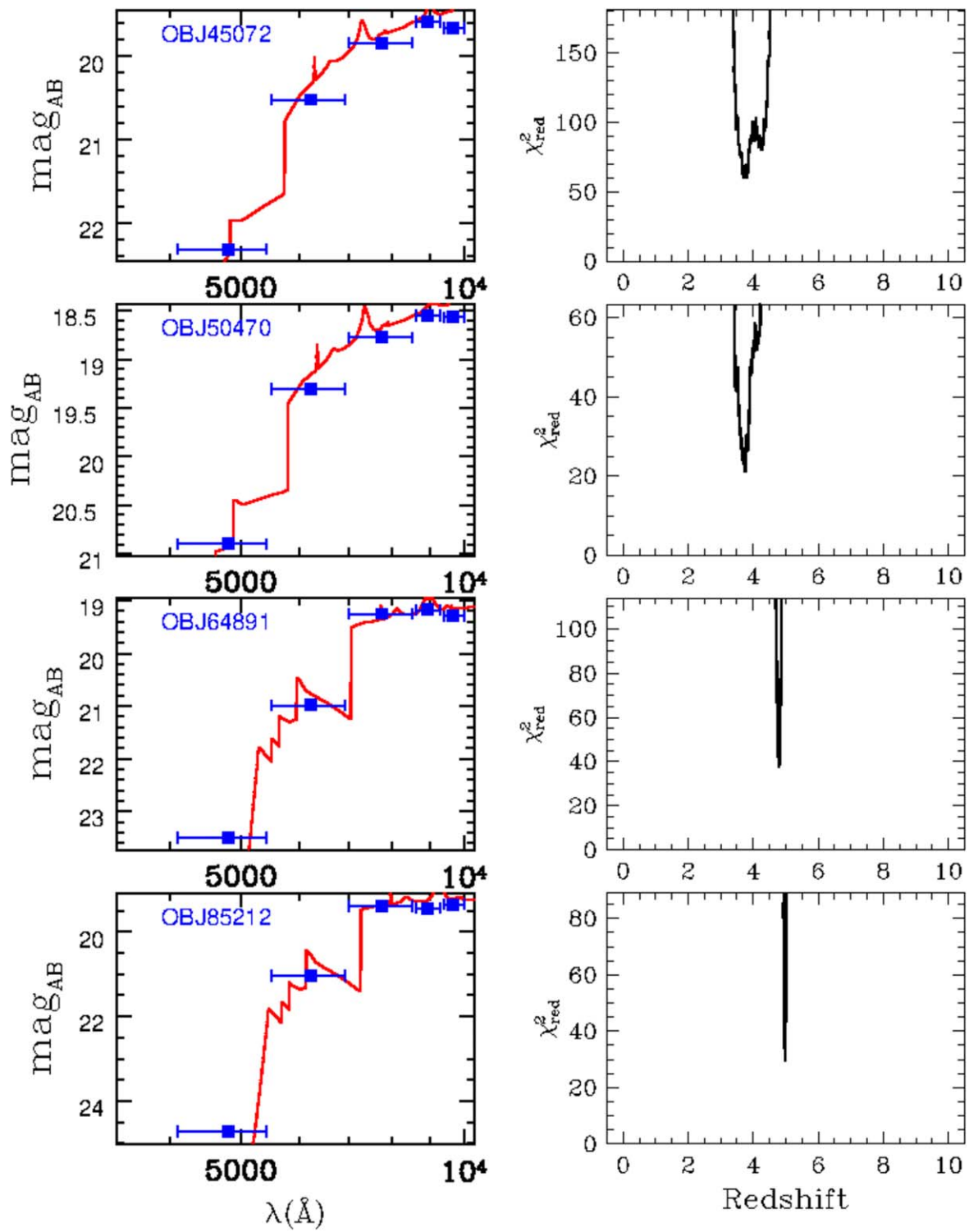
Figure A2. The best-fit SED (left) and the $\chi^2(z_{phot})$ at different redshifts (right) for spectroscopically confirmed QSOs at $z \sim 5$ in the HSC-Wide survey.

Figure A3. The best-fit SED (left) and the $\chi^2(z_{phot})$ at different redshifts (right) for spectroscopically confirmed QSOs at $z \sim 5$ in the HSC-Wide survey.
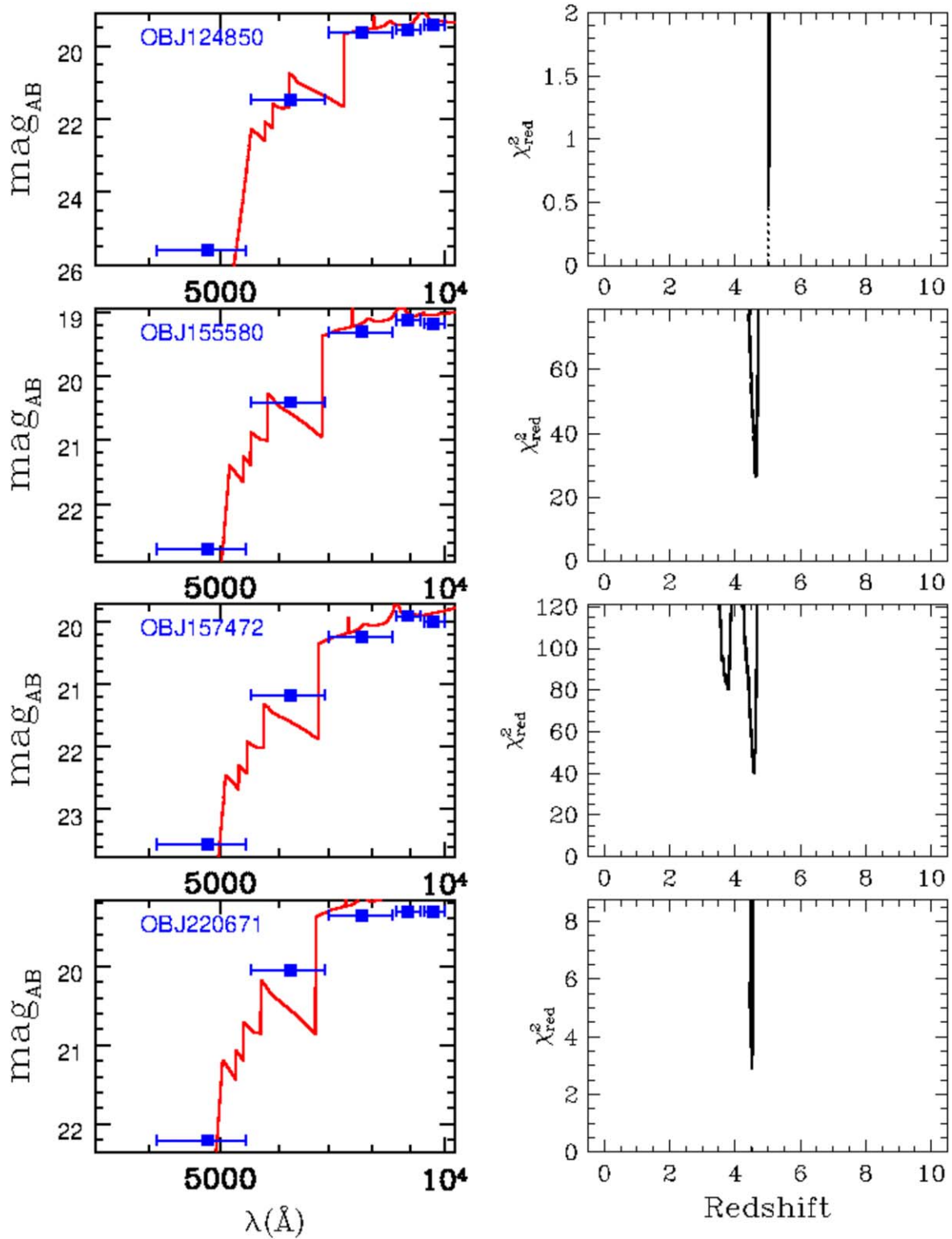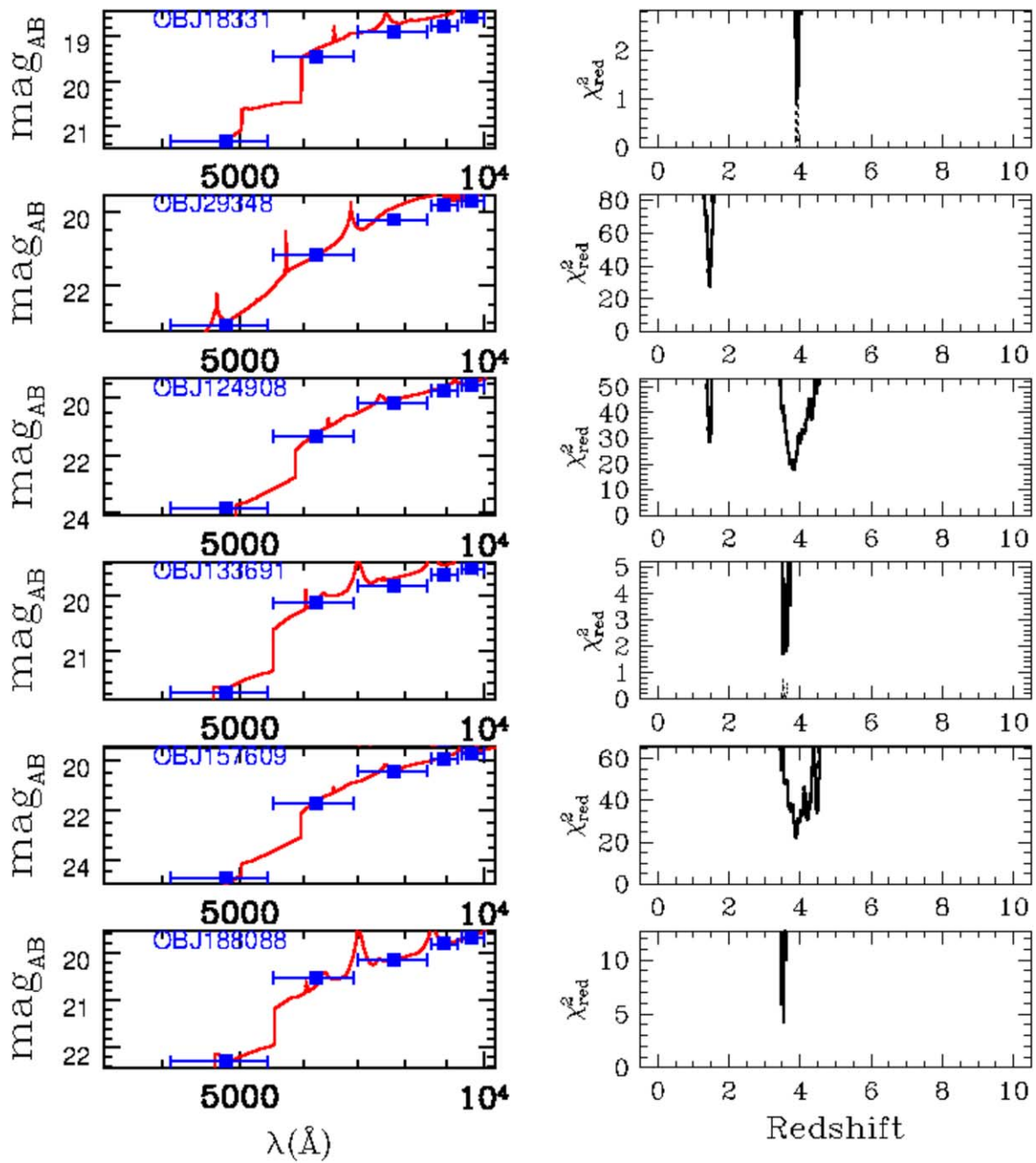
Figure A4. The best-fit SED (left) and the $\chi^2(z_{phot})$ at different redshifts (right) for color-selected QSO candidates in the HSC-Wide survey.

ORCID iDs

Andrea Grazian ⓘ https://orcid.org/0000-0002-5688-0663
Konstantina Boutsia ⓘ https://orcid.org/0000-0003-4432-5037
Emanuele Giallongo ⓘ https://orcid.org/0000-0003-0734-1273
Stefano Cristiani ⓘ https://orcid.org/0000-0002-2115-5234
Fabio Fontanot ⓘ https://orcid.org/0000-0003-4744-0188
Manuela Bischetti ⓘ https://orcid.org/0000-0002-4314-021X
Angela Bongiorno ⓘ https://orcid.org/0000-0002-0101-6624
Giorgio Calderone ⓘ https://orcid.org/0000-0002-7738-5389
Guido Cupani ⓘ https://orcid.org/0000-0002-6830-9093
Valentina D'Odorico ⓘ https://orcid.org/0000-0003-3693-3091
Chiara Feruglio ⓘ https://orcid.org/0000-0002-4227-6035
Fabrizio Fiore ⓘ https://orcid.org/0000-0002-4031-4157
Francesco Guarneri ⓘ https://orcid.org/0000-0003-4740-9762
Matteo Porru ⓘ https://orcid.org/0009-0004-2597-6146
Ivano Saccheo ⓘ https://orcid.org/0000-0003-1174-6978

References

Abdurro'uf, Accetta, K., Aerts, C., et al. 2022, ApJS, 259, 35
Aihara, H., AlSayyad, Y., Ando, M., et al. 2022, PASJ, 74, 247
Akiyama, M., He, W., Ikeda, H., et al. 2018, PASJ, 70, S34
Alam, S., Albareti, F. D., Allende Prieto, C., et al. 2015, ApJS, 219, 12
Barchiesi, L., Dessauges-Zavadsky, M., Vignali, C., et al. 2023, A&A, 675, A30
Becker, G. D., & Bolton, J. S. 2013, MNRAS, 436, 1023
Bolton, J. S., & Haehnelt, M. G. 2007, MNRAS, 382, 325
Bosman, S. E. I., Davies, F. B., Becker, G. D., et al. 2022, MNRAS, 514, 55
Boutsia, K., Grazian, A., Calderone, G., et al. 2020, ApJS, 250, 26
Boutsia, K., Grazian, A., Fontanot, F., et al. 2021, ApJ, 912, 111
Boutsia, K., Grazian, A., Giallongo, E., Fiore, F., & Civano, F. 2018, ApJ, 869, 20
Bouwens, R. J., Illingworth, G. D., Franx, M., & Ford, H. 2007, ApJ, 670, 928
Bouwens, R. J., Illingworth, G. D., Rosati, P., et al. 2003, ApJ, 595, 589
Brinchmann, J. 2023, MNRAS, 525, 2087
Calderone, G., Boutsia, K., Cristiani, S., et al. 2019, ApJ, 887, 268
Calverley, A. P., Becker, G. D., Haehnelt, M. G., & Bolton, J. S. 2011, MNRAS, 412, 2543
Choudhury, T. R. 2022, GReGr, 54, 102
Cristiani, S., Serrano, L. M., Fontanot, F., Vanzella, E., & Monaco, P. 2016, MNRAS, 462, 2478
Davies, F. B., Hennawi, J. F., Bañados, E., et al. 2018, ApJ, 864, 142
Dayal, P., & Ferrara, A. 2018, PhR, 780, 1
Desprez, G., Picouet, V., Moutard, T., et al. 2023, A&A, 670, A82
Eilers, A.-C., Davies, F. B., & Hennawi, J. F. 2018, ApJ, 864, 53
Fan, X., Banados, E., & Simcoe, R. A. 2023, ARA&A, 61, 373
Fan, X., Carilli, C. L., & Keating, B. 2006, ARA&A, 44, 415
Faucher-Giguère, C.-A. 2020, MNRAS, 493, 1614
Finkelstein, S. L., & Bagley, M. B. 2022, ApJ, 938, 25
Finkelstein, S. L., Bagley, M. B., Arrabal Haro, P., et al. 2022, ApJL, 940, L55
Finkelstein, S. L., D'Aloisio, A., Paardekooper, J.-P., et al. 2019, ApJ, 879, 36
Fiore, F., Ferrara, A., Bischetti, M., Feruglio, C., & Travascio, A. 2023, ApJL, 943, L27
Fontanot, F., Cristiani, S., Grazian, A., et al. 2023, MNRAS, 520, 740
Fontanot, F., Cristiani, S., Monaco, P., et al. 2007, A&A, 461, 39
Furusawa, H., Kosugi, G., Akiyama, M., et al. 2008, ApJS, 176, 1
Gaia Collaboration, Vallenari, A., Brown, A. G. A., et al. 2023, A&A, 674, A1
Gaikwad, P., Haehnelt, M. G., Davies, F. B., et al. 2023, arXiv:2304.02038
Gallego, S. G., Cantalupo, S., Sarpas, S., et al. 2021, MNRAS, 504, 16
Gehrels, N. 1986, ApJ, 303, 336
George, E. M., Reichardt, C. L., Aird, K. A., et al. 2015, ApJ, 799, 177
Giallongo, E., Grazian, A., Fiore, F., et al. 2015, A&A, 578, A83
Giallongo, E., Grazian, A., Fiore, F., et al. 2019, ApJ, 884, 19
Giallongo, E., Menci, N., Fiore, F., et al. 2012, ApJ, 755, 124
Glikman, E., Djorgovski, S. G., Stern, D., et al. 2011, ApJL, 728, L26
Grazian, A., Giallongo, E., Boutsia, K., et al. 2018, A&A, 613, A44
Grazian, A., Giallongo, E., Boutsia, K., et al. 2022, ApJ, 924, 62
Grazian, A., Giallongo, E., Fiore, F., et al. 2020, ApJ, 897, 94
Griggio, M., Nardiello, D., & Bedin, L. R. 2023, AN, 344, 20230006
Guarneri, F., Calderone, G., Cristiani, S., et al. 2021, MNRAS, 506, 2471
Harikane, Y., Zhang, Y., Nakajima, K., et al. 2023, arXiv:2303.11946
Haslbauer, M., Kroupa, P., Zonoozi, A. H., & Haghi, H. 2022, ApJL, 939, L31
Hoag, A., Bradač, M., Huang, K., et al. 2019, ApJ, 878, 12
Iani, E., Caputi, K. I., Rinaldi, P., & Kokorev, V. I. 2022, ApJL, 940, L24
Ilbert, O., Arnouts, S., McCracken, H. J., et al. 2006, A&A, 457, 841
Inoue, A. K., Shimizu, I., Iwata, I., & Tanaka, M. 2014, MNRAS, 442, 1805
Jiang, L., Ning, Y., Fan, X., et al. 2022, NatAs, 6, 850
Jin, X., Yang, J., Fan, X., et al. 2023, ApJ, 942, 59
Keating, L. C., Weinberger, L. H., Kulkarni, G., et al. 2020, MNRAS, 491, 1736
Keller, B. W., Munshi, F., Trebitsch, M., & Tremmel, M. 2023, ApJL, 943, L28
Kim, Y., & Im, M. 2021, ApJL, 910, L11
Kim, Y., Im, M., Jeon, Y., et al. 2020, ApJ, 904, 111
Kocevski, D. D., Onoue, M., Inayoshi, K., et al. 2023, ApJL, 954, L4
Kulkarni, G., Worseck, G., & Hennawi, J. F. 2019, MNRAS, 488, 1035
Labbé, I., van Dokkum, P., Nelson, E., et al. 2023, Natur, 616, 266
Larson, R. L., Finkelstein, S. L., Kocevski, D. D., et al. 2023, ApJL, 953, L29
Le Fèvre, O., Cassata, P., Cucciati, O., et al. 2013, A&A, 559, A14
Lehnert, M. D., & Bremer, M. 2003, ApJ, 593, 630
Maiolino, R., Scholtz, J., Witstok, J., et al. 2023, arXiv:2305.12492
Matsuoka, Y., Onoue, M., Iwasawa, K., et al. 2023, ApJL, 949, L42
McGreer, I. D., Fan, X., Jiang, L., & Cai, Z. 2018, AJ, 155, 131
McGreer, I. D., Jiang, L., Fan, X., et al. 2013, ApJ, 768, 105
Meiksin, A. A. 2009, RvMP, 81, 1405
Mitra, S., Choudhury, T. R., & Ferrara, A. 2018, MNRAS, 473, 1416
Naidu, R. P., Tacchella, S., Mason, C. A., et al. 2020, ApJ, 892, 109
Niida, M., Nagao, T., Ikeda, H., et al. 2020, ApJ, 904, 89
Onken, C. A., Wolf, C., Bian, F., et al. 2022, MNRAS, 511, 572
Ono, Y., Harikane, Y., Ouchi, M., et al. 2023, ApJ, 951, 72
Onoue, M., Inayoshi, K., Ding, X., et al. 2023, ApJL, 942, L17
Pan, Z., Jiang, L., Fan, X., Wu, J., & Yang, J. 2022, ApJ, 928, 172
Pâris, I., Petitjean, P., Aubourg, É., et al. 2014, A&A, 563, A54
Parsa, S., Dunlop, J. S., & McLure, R. J. 2018, MNRAS, 474, 2904
Planck Collaboration, Aghanim, N., Akrami, Y., et al. 2020, A&A, 641, A6
Reichardt, C. L., Patil, S., Ade, P. A. R., et al. 2021, ApJ, 908, 199
Robertson, B. E., Tacchella, S., Johnson, B. D., et al. 2023, NatAs, 7, 611
Rodighiero, G., Bisigello, L., Iani, E., et al. 2023, MNRAS, 518, L19
Romano, M., Grazian, A., Giallongo, E., et al. 2019, A&A, 632, A45
Schindler, J.-T., Bañados, E., Connor, T., et al. 2023, ApJ, 943, 67
Schindler, J.-T., Fan, X., Huang, Y.-H., et al. 2019a, ApJS, 243, 5
Schindler, J.-T., Fan, X., McGreer, I. D., et al. 2019b, ApJ, 871, 258
Shin, S., Im, M., Kim, Y., et al. 2020, ApJ, 893, 45
Shin, S., Im, M., & Kim, Y. 2022, ApJ, 937, 32
Spergel, D. N., Verde, L., Peiris, H. V., et al. 2003, ApJS, 148, 175
Trebitsch, M., Dubois, Y., Volonteri, M., et al. 2021, A&A, 653, A154
Trenti, M., & Stiavelli, M. 2008, ApJ, 676, 767
Trinca, A., Schneider, R., Maiolino, R., et al. 2023, MNRAS, 519, 4753
Trinca, A., Schneider, R., Valiante, R., et al. 2022, MNRAS, 511, 616
Trump, J. R., Arrabal Haro, P., Simons, R. C., et al. 2023, ApJ, 945, 35
Übler, H., Maiolino, R., Curtis-Lake, E., et al. 2023, arXiv:2302.06647
Wang, F., Wu, X.-B., Fan, X., et al. 2016, ApJ, 819, 24
Wang, X., Cheng, C., Ge, J., et al. 2022, arXiv:2212.04476
Wolf, C., Onken, C. A., Luvaul, L. C., et al. 2018, PASA, 35, e010
Worseck, G., Prochaska, J. X., O'Meara, J. M., et al. 2014, MNRAS, 445, 1745
Wyithe, J. S. B., & Bolton, J. S. 2011, MNRAS, 412, 1926
Yan, H., Ma, Z., Ling, C., Cheng, C., & Huang, J.-S. 2023, ApJL, 942, L9
Yang, J., Fan, X., Gupta, A., et al. 2023, arXiv:2302.01777
Yang, J., Wang, F., Wu, X.-B., et al. 2016, ApJ, 829, 33
Zhu, Y., Becker, G. D., Bosman, S. E. I., et al. 2022, ApJ, 932, 76